Eur. Phys. J. C manuscript No.
(will be inserted by the editor)

Production of Λ-hyperons in inelastic p+p interactions at 158 GeV/c

A. Aduszkiewicz[16], Y. Ali[14], E. Andronov[22], T. Antićić[3], N. Antoniou[8], B. Baatar[20], F. Bay[24], A. Blondel[26], M. Bogomilov[2], A. Brandin[21], A. Bravar[26], J. Brzychczyk[14], S.A. Bunyatov[20], O. Busygina[19], P. Christakoglou[8], M. Ćirković[23], T. Czopowicz[18], A. Damyanova[26], N. Davis[8], H. Dembinski[5], M. Deveaux[7], F. Diakonos[8], S. Di Luise[24], W. Dominik[16], J. Dumarchez[4], K. Dynowski[18], R. Engel[5], A. Ereditato[25], G.A. Feofilov[22], Z. Fodor[9,17], A. Garibov[1], M. Gaździcki[7,12], M. Golubeva[19], K. Grebieszkow[18], A. Grzeszczuk[15], F. Guber[19], A. Haesler[26], T. Hasegawa[10], A.E. Hervé[5], M. Hierholzer[25], S. Igolkin[22], A. Ivashkin[19], S.R. Johnson[28], K. Kadija[3], A. Kapoyannis[8], E. Kaptur[15], J. Kisiel[15], T. Kobayashi[10], V.I. Kolesnikov[20], D. Kolev[2], V.P. Kondratiev[22], A. Korzenev[26], K. Kowalik[13], S. Kowalski[15], M. Koziel[7], A. Krasnoperov[20], M. Kuich[16], A. Kurepin[19], D. Larsen[14], A. László[9], M. Lewicki[17], V.V. Lyubushkin[20], M. Maćkowiak-Pawłowska[18], B. Maksiak[18], A.I. Malakhov[20], D. Manić[23], A. Marcinek[14,17], A.D. Marino[28], K. Marton[9], H.-J. Mathes[5], T. Matulewicz[16], V. Matveev[20], G.L. Melkumov[20], B. Messerly[30], G.B. Mills[27], S. Morozov[19,21], S. Mrówczyński[12], Y. Nagai[28], T. Nakadaira[10], M. Naskręt[17], M. Nirkko[25], K. Nishikawa[10], A.D. Panagiotou[8], V. Paolone[30], M. Pavin[4,3], O. Petukhov[19,21], C. Pistillo[25], R. Płaneta[14], B.A. Popov[20,4], M. Posiadała[16], S. Puławski[15], J. Puzović[23], W. Rauch[6], M. Ravonel[26], A. Redij[25], R. Renfordt[7], E. Richter-Wąs[14], A. Robert[4], D. Röhrich[11], E. Rondio[13], M. Roth[5], A. Rubbia[24], B.T. Rumberger[28], A. Rustamov[1,7], M. Rybczynski[12], A. Sadovsky[19], K. Sakashita[10], K. Schmidt[15], T. Sekiguchi[10], I. Selyuzhenkov[21], A. Seryakov[22], P. Seyboth[12], D. Sgalaberna[24], M. Shibata[10], M. Słodkowski[18], P. Staszel[14], G. Stefanek[12], J. Stepaniak[13], H. Ströbele[7], T. Šuša[3], M. Szuba[5], M. Tada[10], A. Taranenko[21], D. Tefelski[18], V. Tereshchenko[20], R. Tsenov[2], L. Turko[17], R. Ulrich[5], M. Unger[5], M. Vassiliou[8], D. Veberič[5], V.V. Vechernin[22], G. Vesztergombi[9], L. Vinogradov[22], A. Wilczek[15], Z. Włodarczyk[12], A. Wojtaszek-Szwarc[12], O. Wyszyński[14], L. Zambelli[4,10], E.D. Zimmerman[28]
(NA61/SHINE Collaboration)

[1]National Nuclear Research Center, Baku, Azerbaijan
[2]Faculty of Physics, University of Sofia, Sofia, Bulgaria
[3]Ruđer Bošković Institute, Zagreb, Croatia
[4]LPNHE, University of Paris VI and VII, Paris, France
[5]Karlsruhe Institute of Technology, Karlsruhe, Germany
[6]Fachhochschule Frankfurt, Frankfurt, Germany
[7]University of Frankfurt, Frankfurt, Germany
[8]University of Athens, Athens, Greece
[9]Wigner Research Centre for Physics of the Hungarian Academy of Sciences, Budapest, Hungary
[10]Institute for Particle and Nuclear Studies, Tsukuba, Japan
[11]University of Bergen, Bergen, Norway
[12]Jan Kochanowski University in Kielce, Poland
[13]National Centre for Nuclear Research, Warsaw, Poland
[14]Jagiellonian University, Cracow, Poland
[15]University of Silesia, Katowice, Poland
[16]University of Warsaw, Warsaw, Poland
[17]University of Wrocław, Wrocław, Poland
[18]Warsaw University of Technology, Warsaw, Poland
[19]Institute for Nuclear Research, Moscow, Russia
[20]Joint Institute for Nuclear Research, Dubna, Russia
[21]National Research Nuclear University "MEPhI" (Moscow Engineering Physics Institute), Moscow, Russia
[22]St. Petersburg State University, St. Petersburg, Russia
[23]University of Belgrade, Belgrade, Serbia
[24]ETH Zürich, Zürich, Switzerland
[25]University of Bern, Bern, Switzerland
[26]University of Geneva, Geneva, Switzerland
[27]Los Alamos National Laboratory, Los Alamos, USA
[28]University of Colorado, Boulder, USA
[29]University of Pittsburgh, Pittsburgh, USA
[30]*Present address:* Department of Physics, COMSATS Institute of Information Technology, Islamabad 44000 Pakistan
§ Corresponding author: Tatjana.Susa@irb.hr

Received: date / Revised version: date

arXiv:1510.03720v4 [hep-ex] 25 Apr 2016

Abstract Inclusive production of Λ-hyperons was measured with the large acceptance NA61/SHINE spectrometer at the CERN SPS in inelastic p+p interactions at beam momentum of 158 GeV/c. Spectra of transverse momentum and transverse mass as well as distributions of rapidity and x_F are presented. The mean multiplicity was estimated to be $0.120 \pm 0.006\ (stat.) \pm 0.010\ (sys.)$. The results are compared with previous measurements and predictions of the EPOS, URQMD and FRITIOF models.

1 Introduction

Hyperon production in proton-proton (p+p) interactions has been studied in a long series of fixed target and collider experiments. However, the resulting experimental data suffers from low statistics, incomplete beam momentum coverage, and large differences between the measurements reported by different experiments. Also popular models of proton-proton interactions mostly fail to reproduce the measurements. The data on Λ production and the model predictions are reviewed at the end of this paper.

At the same time rather impressive progress was made in measurements of hyperon production in nucleus-nucleus (A+A) collisions [1]. This has two reasons. Firstly, mean multiplicities of all hadrons in central heavy ion collisions are typically two to three orders of magnitude higher than the corresponding multiplicities in inelastic p+p interactions. Secondly, the hyperon yields per nucleon are enhanced by substantial factors in A+A collisions with respect to p+p interactions. This enhancement, which increases with the strangeness content of the hyperon in question, has raised considerable interest over the past decades. It has in particular been brought into connection with production of the Quark-Gluon Plasma, a 'deconfined' state of matter at that time hypothetical [2, 3]. Nowadays, for the energies well below the LHC energy range, nucleus-nucleus collisions are investigated mainly to find the critical point of strongly interacting matter as well as to study the properties of the onset of deconfinement [4, 5]. In particular, precise measurements of inclusive hadron production properties as a function of beam momentum (13A-158A GeV/c) and size of colliding nuclei (p+p, p+Pb, Be+Be, Ar+Sc, Xe+La) are performed by NA61/SHINE [6]. Results on inelastic p+p interactions are an important part of this scan.

NA61/SHINE already published results on $\pi^{\pm}$, $K^{\pm}$, proton, Λ and K^0_S production in p+C interactions at beam momentum of 31 GeV/c [7–10], as well as π^- production in p+p collisions at 20-158 GeV/c [11].

This paper presents the first NA61/SHINE results on strange particle production in p+p interactions. Since all Σ^0 hyperons decay electromagnetically via $\Sigma^0 \to \Lambda\gamma$, which is indistinguishable from direct Λ production, Λ in the following denotes the sum of both Λ directly produced in strong p+p interactions and Λ from decays of Σ^0 hyperons produced in these interactions.

The particle rapidity is calculated in the collision centre of mass system (cms): $y = \mathrm{atanh}(\beta_{\mathrm{L}})$, where $\beta_{\mathrm{L}} = p_{\mathrm{L}}/E$ is the longitudinal component of the velocity, p_{L} and E are longitudinal momentum and energy in the cms and $x_{\mathrm{F}} = p_{\mathrm{L}}/p_{beam}$ is Feynman's scaling variable with p_{beam} the incident proton momentum in the cms. The transverse component of the momentum is denoted as p_{T} and the transverse mass m_{T} is defined as $m_{\mathrm{T}} = \sqrt{m^2 + p_{\mathrm{T}}^2}$, where m is the particle mass. The collision energy per nucleon pair in the centre of mass system is denoted as $\sqrt{s_{\mathrm{NN}}}$.

2 The experimental setup

The NA61/SHINE experiment [6] uses a large acceptance hadron spectrometer located in the H2 beam-line at the CERN SPS accelerator complex. The layout of the experiment is schematically shown in Fig. 1. Hereby we describe only the components relevant for the analysis. The main detector system is a set of large volume Time Projection Chambers (TPCs). Two of them (VTPC-1 and VTPC-2) are placed inside super-conducting magnets (VTX-1 and VTX-2) with a combined bending power of 9 Tm. The standard current setting for data taking at 158 GeV/c corresponds to full field, 1.5 T, in the first and reduced field, 1.1 T, in the second magnet. Two large TPCs (MTPC-L and MTPC-R) are positioned downstream of the magnets, symmetrically to the undeflected beam. A fifth small TPC (GAP-TPC) is placed between VTPC-1 and VTPC-2 directly on the beam line and covers the gap between the sensitive volumes of the other TPCs. The NA61/SHINE TPC system allows a precise measurement of the particle momenta p with a resolution of $\sigma(p)/p^2 \approx (0.3-7)\times10^{-4}\ (\mathrm{GeV/c})^{-1}$ at the full magnetic field used for data taking at 158 GeV/c and provides particle identification via the measurement of the specific energy loss, dE/dx, with relative resolution of about 4.5%.

A set of scintillation and Cherenkov counters, as well as beam position detectors (BPDs) upstream of the main detection system provide a timing reference, as well as identification and position measurements of the incoming beam particles. The 158 GeV/c secondary hadron beam was produced by 400 GeV/c primary protons impinging on a 10 cm long beryllium target. Hadrons produced at the target are transported downstream to the NA61/SHINE experiment by the H2 beamline, in which collimation and momentum selection occur. Protons from the secondary hadron beam are identified by a differential Cherenkov Counter (CEDAR) [12]. Two scintillation counters, S1 and S2, together with the three veto counters V0, V1 and V1^p were used to select beam particles. Thus, beam particles were required to satisfy the coincidence $S1 \cdot S2 \cdot \overline{V0} \cdot \overline{V1} \cdot \overline{V1^p}$·CEDAR in order

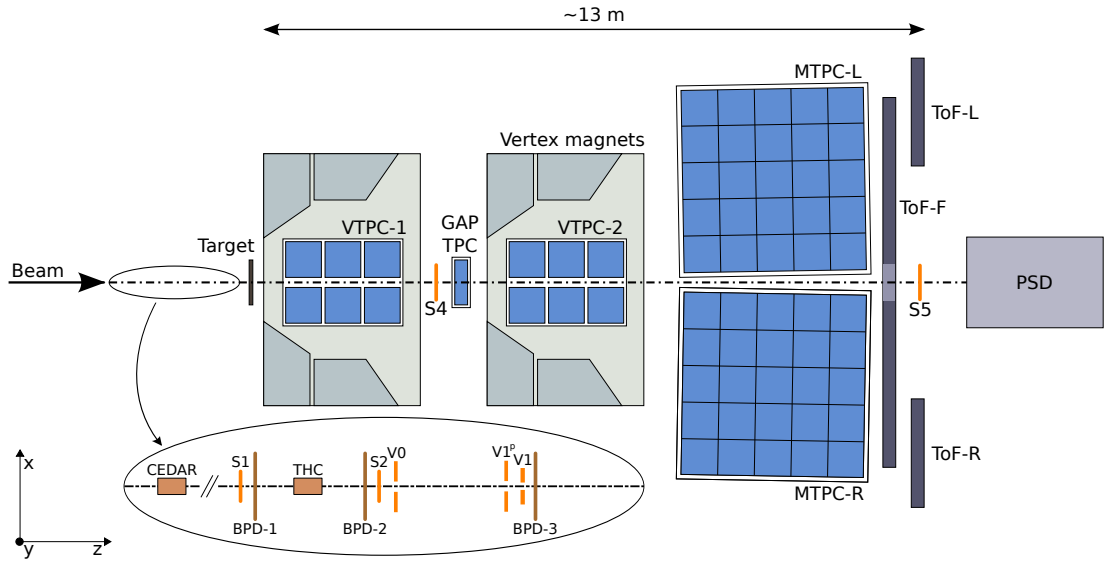

Fig. 1 Schematic layout of the NA61/SHINE experiment at the CERN SPS (horizontal cut in the beam plane, not to scale). The beam and trigger counter configuration used for data taking on p+p interactions in 2009 is presented. The chosen right-handed coordinate system is shown on the plot. The incoming beam direction is along the z axis. The magnetic field bends charged particle trajectories in the x-z (horizontal) plane. The drift direction in the TPCs is along the y (vertical) axis [6]. See details in Section 2.

to become accepted as a valid proton. Trajectories of individual beam particles were measured in a telescope of beam position detectors placed along the beam line (BPD-1/2/3 in Fig. 1). These are multiwire proportional chambers with two orthogonal sense wire planes and cathode strip readout, allowing to determine the transverse coordinates of the individual beam particle at the target position with a resolution of about 100 μm. For data taking on p+p interactions a liquid hydrogen target (LHT) of 20.29 cm length (2.8% interaction length) and 3 cm diameter was placed 88.4 cm upstream of VTPC-1. Data taking with inserted and removed liquid hydrogen (LH) in the LHT was alternated in order to calculate a data-based correction for interactions with the material surrounding the liquid hydrogen. Interactions in the target are selected by requiring an anti-coincidence of the selected beam protons with the signal from a small scintillation counter of 2 cm diameter (S4) placed on the beam trajectory between the two spectrometer magnets. Further details on the experimental setup, beam and the data acquisition can be found in Ref. [6].

3 Analysis technique

In the following section the analysis technique is described, starting with the event reconstruction followed by the event and V^0 selections. Next the Λ signal extraction and the calculation of Λ-yields are presented. Then the correction procedure and the estimation of statistical and systematic uncertainties are discussed. Finally quality tests are performed on the final results. More details can be found in Ref. [13].

3.1 Track and main vertex reconstruction

The main steps of the track and vertex reconstruction procedure are:

(i) cluster finding in the TPC raw data, calculation of the cluster centre-of-gravity and total charge,
(ii) reconstruction of local track segments in each TPC separately,
(iii) matching of track segments into global tracks,
(iv) track fitting through the magnetic field and determination of track parameters at the first measured TPC cluster,
(v) determination of the interaction vertex using the beam trajectory (x and y coordinates) fitted in the BPDs and the trajectories of tracks reconstructed in the TPCs (z coordinate),
(vi) matching of ToF hits with the TPC tracks.

3.2 Event selection

A total of 3.5×10^6 events recorded with the LH inserted (denoted I) and 0.43×10^6 with the LH removed from the target (denoted R) were used for the analysis. The two configurations were realised by filling the target vessel with LH and emptying it.

Interaction events were selected by the following requirements:

(i) no off-time beam particle was detected 1 μs before and after the trigger particle,

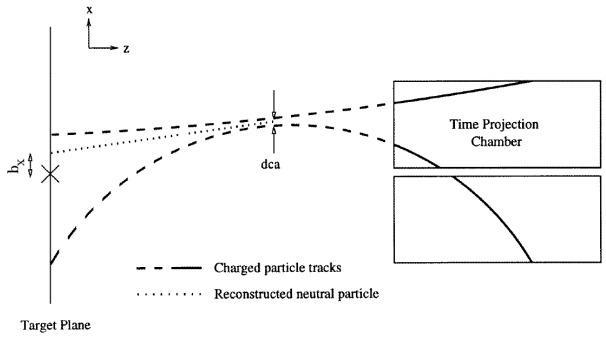

Fig. 2 Definition of distance of the closest approach (dca), and b_x. The variable b_y is defined on the yz-plane in analogy with b_x. The target plane is defined as the plane parallel to the xy-plane containing the main vertex marked with a cross (taken from Ref. [14]).

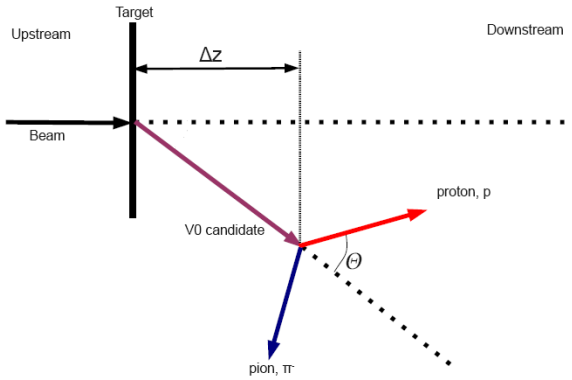

Fig. 3 Definition of Δz variable used for the V^0 selection (see text).

(ii) the trajectory of the beam particle was measured in at least one of BPD-1 or BPD-2 and in the BPD-3 detector and was well reconstructed (BPD-3 is positioned close to and upstream of the LHT),
(iii) the fit of the z-coordinate of the primary interaction vertex converged and the fitted z position is found within ± 40 cm of the centre of the LHT.

The number of events after these selections ($N^I = 1.66 \times 10^6$ for the LH inserted configuration of the target, $N^R = 43 \times 10^3$ for the LH removed) is treated as the raw number of recorded inelastic events.

3.3 V^0 reconstruction and selection

Λ hyperons are identified by reconstructing their decay topology $\Lambda \to p + \pi^-$ (branching ratio 63.9%). In the first step pairs were formed from all measured positively and negatively charged particles. V^0 candidates were required to have a distance of closest approach (dca, Fig. 2) between the two trajectories of less than 1 cm anywhere between the position of the first measured points on the tracks and the primary vertex. In the second step, the position of the secondary vertex and the momenta of the decay tracks were fitted by performing a 9-parameter χ^2 fit employing the Levenberg-Marquardt fitting procedure [15, 16]. In the fit the fitted secondary vertex was added as the first point to the tracks at which the momenta were recalculated. Finally, for each candidate the invariant mass was calculated assuming proton (pion) mass for positively (negatively) charged particles. To ensure a good momentum determination and reduce the combinatorial background from random pairs, a set of quality cuts was imposed:

(i) For each track, the minimum number of clusters in at least one of VTPC-1 and VTPC-2 was required to be 15.
(ii) Proton and pion candidates were selected by requiring their specific energy loss measured by the TPCs to be within 3 σ around the nominal Bethe-Bloch value. This cut was applied only to experimental data.
(iii) For the simulated data (see below) the background was totally discarded by matching, i.e. by using only those reconstructed tracks which were identified as originating from the corresponding Λ decay. The identification was performed by matching the clusters found in the TPCs with the clusters generated in the simulation. In case more than one reconstructed track was matched to a Λ decay daughter the one with the largest number of matched clusters was selected.
(iv) The combinatorial background concentrated in the vicinity of the primary vertex is reduced by imposing a distance cut on the difference between the z coordinate of the primary and Λ vertex ($\Delta z = z_\Lambda - z_{primary}$, see Fig. 3). To maximise the fraction of rejected background while minimising the number of lost Λ candidates, a rapidity dependent cut was applied: $\Delta z > 10$ cm for $y < 0.25$, $\Delta z > 15$ cm for $y \in [0.25, 0.75]$, $\Delta z > 40$ cm for $y \in [0.75, 1.25]$, and $\Delta z > 60$ cm for higher rapidities.
(v) A further significant part of the background (e.g. pairs from photon conversions) was rejected by imposing a cut on $\cos\phi$, where ϕ is defined as the angle between the vectors y', and n, where y' is the vector perpendicular to the momentum of the V^0-particle which lies in the plane spanned by the y-axis and the V^0-momentum vector, and n is a vector normal to the decay plane (see Fig. 4). A rapidity dependent cut was used: $|\cos\phi| < 0.95$ for $y < -0.25$, $|\cos\phi| < 0.9$ for $y \in [-0.25, 0.75]$, $|\cos\phi| < 0.8$ for higher rapidities.
(vi) The trajectories of the Λ candidates were calculated using the decay vertex and the momentum vectors of the decay particles. Extrapolation back to the primary vertex plane resulted in impact parameters b_x (in the magnetic bending plane) and b_y (see Fig. 2). As

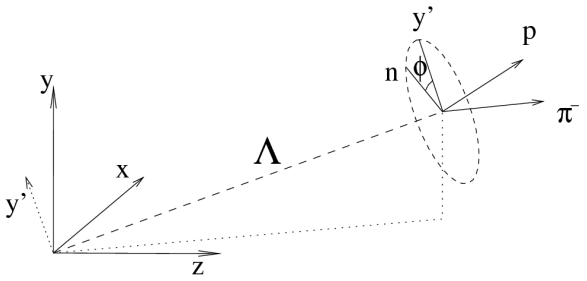

Fig. 4 Definition of ϕ-variable used for the V^0 selection (see text).

the resolution of impact parameters is approximately twice better in y than in x direction, an elliptic cut $\sqrt{(b_x/2)^2+b_y^2} < 1$ cm was imposed in order to reduce the background from Λ candidates which do not originate from the primary vertex.

The selection cuts lead to a high degree of purification of the Λ signal. This is demonstrated by the Armenteros-Podolanski plots [17] of Fig. 5 in which the Λ decays populate the ellipses on the lower right.

3.4 Signal extraction

The raw yield of Λ hyperons was obtained by performing a fit of the invariant mass spectra with the sum of a background and a signal function. The shape of the Λ signal was described by the Lorentzian function:

$$L(m) = A\frac{\frac{1}{2}\Gamma}{(m-m_0)^2+\left(\frac{1}{2}\Gamma\right)^2}, \qquad (1)$$

where m is the invariant mass of the candidate $(p\pi^-)$ pair, A is a normalisation factor, m_0 is the mass parameter and Γ is the FWHM (full width at half maximum) of the Λ peak. As the natural width of Λ decay is negligible, the observed width of the Λ peak is caused almost solely by the detector response. In the standard approach, the background was represented by a Chebyshev polynomial of 2^{nd} order. The uncertainty introduced by choosing this particular functional form was estimated by trying other background functions (see Sec. 3.6).

The sum of the Lorentzian and the background function was fitted in the mass range from 1.080 (1.076 for $y = 0.5$, 1.073 for $y = 1.0$) to 1.250 GeV/c^2. In order to ensure the stability of the fit results, even in the case of low statistics, a three step procedure was developed. In the first step, a pre-fit was performed in order to estimate the initial parameters of the background function. For that purpose, the invariant mass region containing the Λ peak (1.100-1.135 GeV/c^2) was excluded from the fit. In the second step,

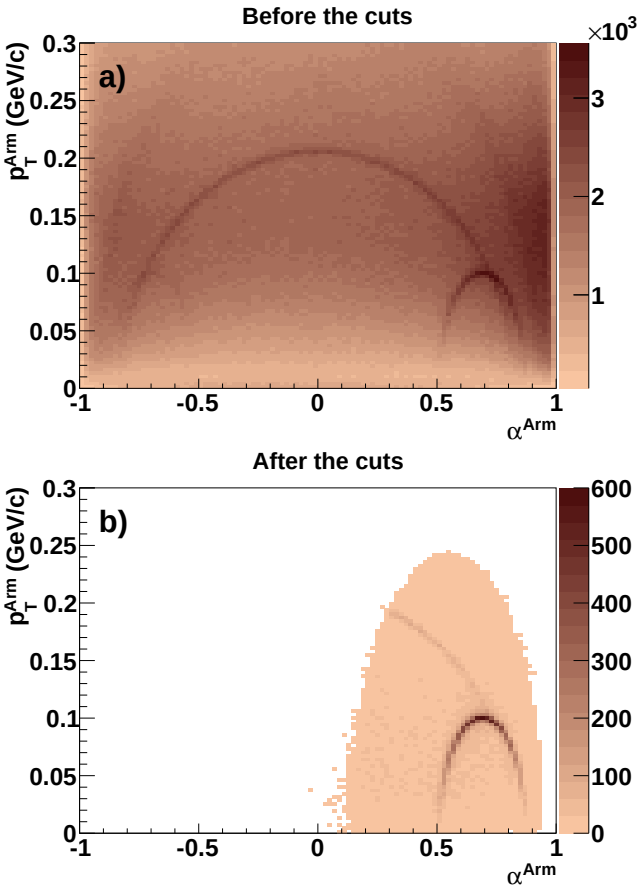

Fig. 5 Armenteros-Podolanski plot for reconstructed V^0 decays before the Λ candidate selection cuts (a), and after the cuts are applied (b). The shading indicates the number of entries per bin. The axis variables are: p_T^{Arm}, the transverse momentum of the decay particles with respect to the direction of motion of the V^0 and $\alpha^{Arm} = (p_L^+ - p_L^-)/(p_L^+ + p_L^-)$ where p_L^+ and p_L^- are the longitudinal momenta of the positive and negative decay particle respectively.

the invariant mass spectrum was fitted to the sum of the signal and the background. The initial values for the parameters of the background function were taken from the first step, while the mass parameter m_0 was fixed to the PDG value $m_\Lambda = 1.115683$ GeV/c^2 [18] and the width was set to 3 MeV. The obtained values were used as the initial parameters for the third step, where no parameter was fixed. The invariant mass distribution of the Λ candidates for the intervals $y \in [-0.75,-0.25]$ and $p_T \in [0.2,0.4]$ GeV/c, together with the result of the final fit is shown in Fig. 6. For the data set with LH inserted, the fits were performed in (k,l) bins, where k stands for the bin in rapidity y or Feynman x_F, and l for the bin in transverse momentum p_T or transverse mass $m_T - m_\Lambda$. The raw number of Λ-hyperons ($n^I(k,l)$) was then obtained by subtracting the fitted background and integrating the remaining signal distributions in the mass window $m_0 \pm 3\Gamma$ (see Fig. 7), where m_0 is the fitted Λ mass. The low statistics of the LH removed data set, forced to restrict the fits to y (x_F) bins summed over the transverse variable,

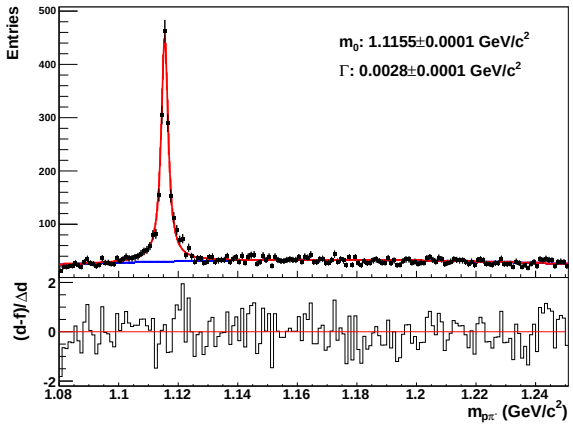

Fig. 6 The invariant mass distribution of Λ candidates for $y \in [-0.75,-0.25]$ and $p_T \in [0.2,0.4]$ GeV/c is shown in the upper plot (LH inserted). The solid line shows a fit to signal plus background, while the dashed line represents the background contribution. The lower part of the plot shows the difference between the data points and the fit, normalised to the statistical error of the data points.

resulting in $n^R(k)$. In order to obtain the raw number of Λ-hyperons in (k,l) bins, it was assumed that the shape of the p_T distributions and the efficiencies for a given y (x_F) bin were the same for the two data sets, and $n^R(k,l)$ was calculated as $n^R(k,l) = n^R(k)\frac{n^I(k,l)}{\sum_l n^I(k,l)}$.

3.5 Correction factors

In order to determine the number of Λ hyperons produced in inelastic p+p interactions, three corrections were applied to the extracted raw number of Λ hyperons:

1. The contribution from interactions in the material outside of the liquid hydrogen volume of the target was subtracted:

$$\frac{n^I(k,l) - Bn^R(k,l)}{N^I - BN^R}. \quad (2)$$

The normalisation factor B was derived by comparing the distribution of the fitted z coordinate of the interaction vertex far away from the target [9] for filled and empty target vessel:

$$B = \frac{N^I_{far\,z}}{N^R_{far\,z}} = 3.93\,, \quad (3)$$

where $N^I_{far\,z}$ ($N^R_{far\,z}$) is the number of events in the region $100 < z < 280$ cm downstream of the target centre for the data sample with inserted (removed) hydrogen in the target vessel.

2. The loss of the Λ hyperons due to the dE/dx requirement, was corrected by a constant factor

$$c_{\mathrm{d}E/\mathrm{d}x} = \frac{1}{\varepsilon^2} = 1.005\,, \quad (4)$$

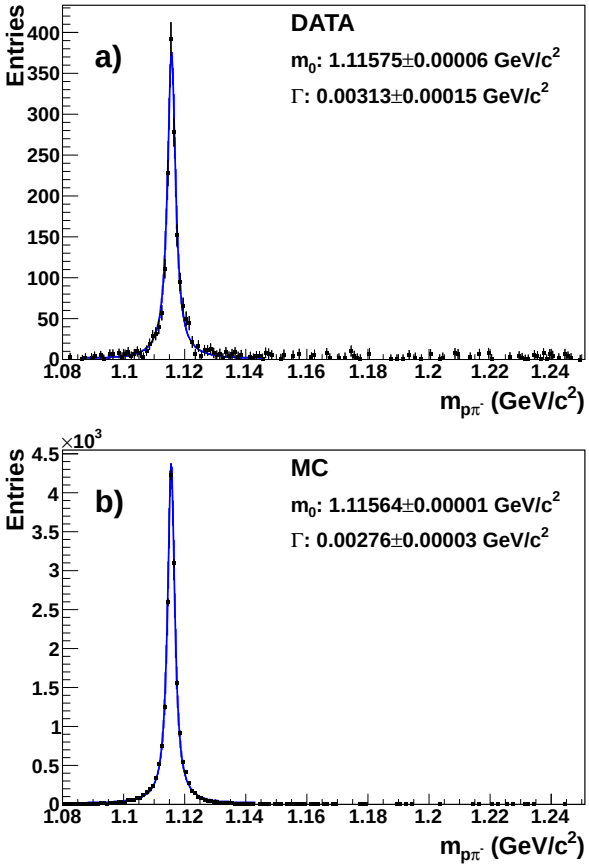

Fig. 7 The invariant mass distribution of Λ candidates for $y \in [-0.25,0.25]$ and $p_T \in [0.2,0.4]$ GeV/c with the LH inserted after subtraction of the fitted background (a), and for the simulation (b).

where $\varepsilon = 0.9973$ is the probability for the proton (pion) to lie within 3σ around the nominal Bethe-Bloch value.

3. A detailed Monte Carlo simulation was performed to correct for geometrical acceptance, reconstruction efficiency, losses due to the trigger bias, the branching ratio of the Λ decay, the feed-down from hyperon decays as well as the quality cuts applied in the analysis. The correction factors are based on 20×10^6 inelastic p+p events produced by the EPOS1.99 event generator [19]. The particles in the generated events were tracked through the NA61/SHINE apparatus using the GEANT3 package [20]. The TPC response was simulated by dedicated NA61/SHINE software packages which take into account all known detector effects. The simulated events were reconstructed with the same software as used for real events and the same selection cuts were applied (except the identification cut). As seen from Fig. 7 the shape and position of the Λ peak is well reproduced by the simulation while the width is about 10% narrower. More details on MC validation can be found in Ref. [11].

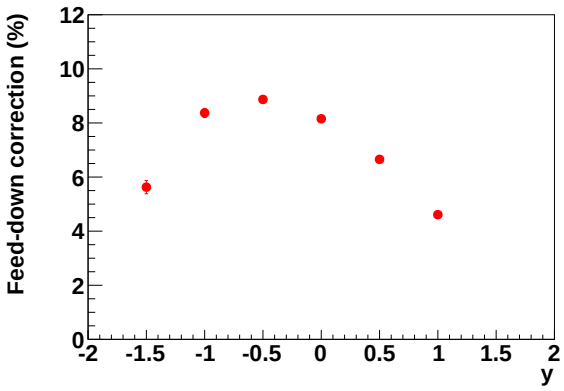

Fig. 8 Feed-down correction: the contribution from Ξ^- and Ξ^0 to total Λ decays calculated using EPOS1.99 model.

For each (k,l) bin, the correction factor $c_{MC}(k,l)$ was calculated as

$$c_{MC}(k,l) = \frac{n^{gen}_{MC}(k,l)}{N^{gen}_{MC}} \Bigg/ \frac{n^{acc}_{MC}(k,l)}{N^{acc}_{MC}}\,, \tag{5}$$

where

- $n^{gen}_{MC}(k,l)$ is the number of Λ hyperons produced in a given (k,l) bin in the primary interactions, including Λ hyperons from the Σ^0 decays,
- $n^{acc}_{MC}(k,l)$ is the number of reconstructed Λ hyperons in a given (k,l) bin, determined by matching the reconstructed Λ candidates to the simulated Λ hyperons based on the cluster positions,
- N^{gen}_{MC} is the number of generated inelastic p+p interactions ($19\,961 \times 10^3$),
- N^{acc}_{MC} is the number of accepted p+p events ($15\,607 \times 10^3$),
- $k = y$ or x_F, and $l = p_T$ or $m_T - m_\Lambda$.

These factors also include the correction for feed-down from weak decays (mostly of Ξ^- and Ξ^0, see Fig. 8). The Ξ^- yields as function of rapidity generated by the EPOS1.99 simulation agree within 10% with the measurements reported in Ref. [21]. The values of the correction factors are presented in Fig. 9.

Statistical errors of the correction factors were calculated using the following approach: The correction factor (c_{MC}) consists of two parts:

$$\begin{aligned} c_{MC}(k,l) &= \frac{n^{gen}_{MC}(k,l)}{N^{gen}_{MC}} \Bigg/ \frac{n^{acc}_{MC}(k,l)}{N^{acc}_{MC}} \\ &= \frac{N^{acc}_{MC}}{N^{gen}_{MC}} \Bigg/ \frac{n^{acc}_{MC}(k,l)}{n^{gen}_{MC}(k,l)} = \frac{\alpha}{\beta(k,l)}\,, \end{aligned} \tag{6}$$

where α describes the loss of inelastic events due to the event selection, and β takes into account the loss of Λ hyperons due to the V^0-cuts, efficiency, and the other aforementioned effects.

The error of α was calculated assuming a binomial distribution, while the part β involving the fitting procedure takes into account the error of the fit:

$$\Delta\alpha = \sqrt{\frac{\alpha(1-\alpha)}{N^{gen}_{MC}}}, \tag{7}$$

$$\Delta\beta(k,l) = \sqrt{\left(\frac{\Delta n^{acc}_{MC}(k,l)}{n^{gen}_{MC}(k,l)}\right)^2 + \left(\frac{n^{acc}_{MC}(k,l)\Delta n^{gen}_{MC}(k,l)}{(n^{gen}_{MC}(k,l))^2}\right)^2}, \tag{8}$$

where $\Delta n^{acc}_{MC}(k,l)$ is the uncertainty of the fit, and $\Delta n^{gen}_{MC}(k,l) = \sqrt{n^{gen}_{MC}(k,l)}$. The total statistical error of c_{MC} was calculated as follows:

$$\Delta c_{MC} = \sqrt{\left(\frac{\Delta\beta}{\alpha}\right)^2 + \left(-\frac{\beta\Delta\alpha}{\alpha^2}\right)^2}\,. \tag{9}$$

Finally, the double-differential yield of Λ hyperons per inelastic event in a bin (k,l) amounts to:

$$\frac{d^2n}{dkdl} = \frac{c_{dE/dx}c_{MC}(k,l)}{\Delta k \Delta l} \frac{n^I(k,l) - Bn^R(k,l)}{N^I - BN^R}\,, \tag{10}$$

with

- $n^{I/R}$ the uncorrected number of Λ hyperons for the hydrogen inserted/removed target configurations,
- $N^{I/R}$ the number of events for the hydrogen inserted/removed data after event cuts,
- $c_{dE/dx}$, c_{MC} the correction factors described in Sec. 3.5,
- B the normalisation factor (defined in Sec. 3.5),
- $k = y$ or x_F, and $l = p_T$ or $m_T - m_\Lambda$,
- Δk and Δl the bin widths.

3.6 Statistical and systematic uncertainties

The statistical errors of the corrected double differential yields (see Eq. 10) take into account the statistical errors of c_{MC} (see Eq. (9)) and the statistical errors on the fitted Λ yields in the LH inserted and removed configurations. The statistical errors on B and $c_{dE/dx}$ were neglected.

The systematic uncertainties were estimated taking into account four sources. For each source modifications to the standard analysis procedure were applied and the deviation of the results from the standard procedure were calculated. As the effects of the modifications are partially correlated, the maximal positive and negative deviation from the standard procedure was determined for each bin and source separately. Then, the positive (negative) systematic uncertainties were calculated separately by adding

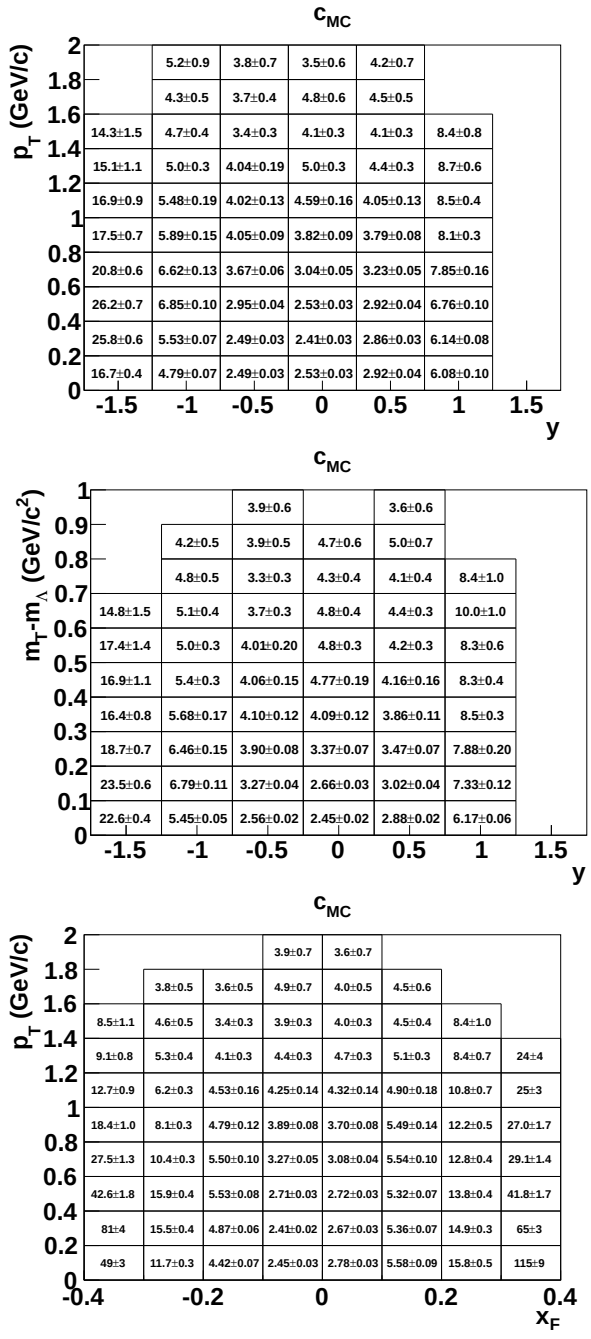

Fig. 9 Correction factors c_{MC} for binning in (y, p_T) at top, $(y, m_T - m_\Lambda)$ at centre and (x_F, p_T) at bottom. The error Δc_{MC} ranges from 0.02 to 1.48 for binning in (y, p_T) and (y, m_T), and from 0.02 to 8.70 for (x_F, p_T).

in quadrature the positive (negative) contribution from each source.

The considered sources of the systematic uncertainty and the corresponding modifications of the standard method were the following:

(i) The uncertainty due to the signal extraction procedure:

- The standard function used for background fit, a Chebyshev polynomial of 2^{nd} order, was changed for a Chebyshev polynomial of 3^{rd} order and for a standard polynomial of 2^{nd} order.
- The range within which the raw number of Λ particles is summed up was changed from 3Γ to 2.5Γ and 3.5Γ.
- The lower limit of the fitting range was changed from 1.08 GeV/c^2 (1.076 for $y = 0.5$, 1.073 for $y = 1.0$) to 1.083 GeV/c^2 (1.079 for $y = 0.5$, 1.076 for $y = 1.0$).
- The initial value of the Γ parameter of the signal function was changed by ± 8 %.
- the initial value for the mass parameter of the Lorentz function was changed by ± 0.3 MeV.

(ii) The effect of the event and quality cuts were checked by performing the analysis with the following cuts changed compared to the values presented in Secs. 3.2 and 3.3.

- The cut on the z-position of the interaction vertex was changed from ± 40 cm to ± 30 cm and ± 50 cm with respect to the centre of the target.
- The window in which off-time beam particles are not allowed was increased from 1 μs to 1.5 μs.
- The elliptic cut on the impact parameters was reduced by a factor of 2: $\sqrt{b_x^2 + (2b_y)^2} < 1$ cm.
- The dE/dx cut was modified to $\pm 2.8\sigma$ or 3.2σ to estimate possible systematic effects of dE/dx calibration.
- The matching procedure used to reject background in the simulation was turned off.
- The required minimal number of charge clusters in at least one of the VTPCs for both V^0-decay products was decreased to 12 or increased to 18.
- The cut on Δz, the distance between the decay and the primary interaction vertex, was changed from the standard values to the values shown in columns A and B in the following table:

Minimal Δz (cm) allowed				
y_{min}	y_{max}	standard	A	B
-1.75	0.25	10	7.5	12.5
0.25	0.75	15	11.25	18.75
0.75	1.25	40	30	50

- The limits for the cut on $\cos\phi$ were changed from the standard values to the values shown in columns A and B in the following table:

Maximal $\lvert\cos\phi\rvert$ allowed				
y_{min}	y_{max}	standard	A	B
-1.75	-0.25	0.95	0.975	0.925
-0.25	0.75	0.9	0.95	0.85
0.75	1.25	0.8	0.85	0.75

(iii) In order to find the systematic uncertainty of the normalisation factor B in Eq. (3) for the LH removed configuration, the limits of the region for which this parameter was calculated was varied in steps of 0.1 m. For each combination of the lower limit (ranging from 0.8 to 1.8 m from the target) and upper limit in z (from 2.8 m to 3.8 from the target) the B-factor was calculated. The smallest and the highest value of B obtained in this way is taken as the systematic uncertainty range of B.

(iv) For estimation of the uncertainty due to the feed-down correction a conservative systematic uncertainty of 30% on the Ξ^- and Ξ^0 yields predicted by EPOS1.99 was assumed.

The systematic uncertainties are shown in the figures as light blue shaded bars. They are asymmetric (larger downward) mainly due to the differences between the results with or without track matching and the change of the background function to a Chebyshev polynomial of 3^{rd} order. For both changes the shift of the results increases with rapidity.

The distribution of the proper life-time of Λ hyperons was obtained using an analysis procedure analogous to the one presented in Sec. 4. The data for the lifetime analysis were binned in rapidity $k = y$ (from -1.5 to +1.0, in steps of 0.5) and life-time normalised to the mean life-time t/τ_{PDG} [18] (from 0.00 to 4.75, in steps of 0.25) with $c\tau_{PDG} = 7.89$ cm. The life-time was calculated using the distance r between the V^0-decay vertex and the interaction vertex of the V^0-candidates ($t = r/(\gamma\beta)$, where γ, β are the Lorentz variables). Then $d^2n/(dydt)$ was calculated and an exponential function was fitted to the life-time distribution for each rapidity bin separately (see the example in Fig. 10 (a) for $y = -1.0$). The ratio of the fitted mean life-time τ to the corresponding PDG value τ_{PDF} is shown in Fig. 10 (b) as a function of rapidity. The fitted mean life-times are seen to agree with the PDG value for all rapidities indicating good accuracy of the correction procedure.

The expected forward-backward symmetry of the data was also checked. The final double- and single-differential distributions used for this test were found to agree for the corresponding backward and forward rapidities within the statistical errors.

In addition, the stability of results in different periods during the data taking was investigated. For that purpose, the data set was divided into two subsets, containing runs from the first and the second half of the data taking period.

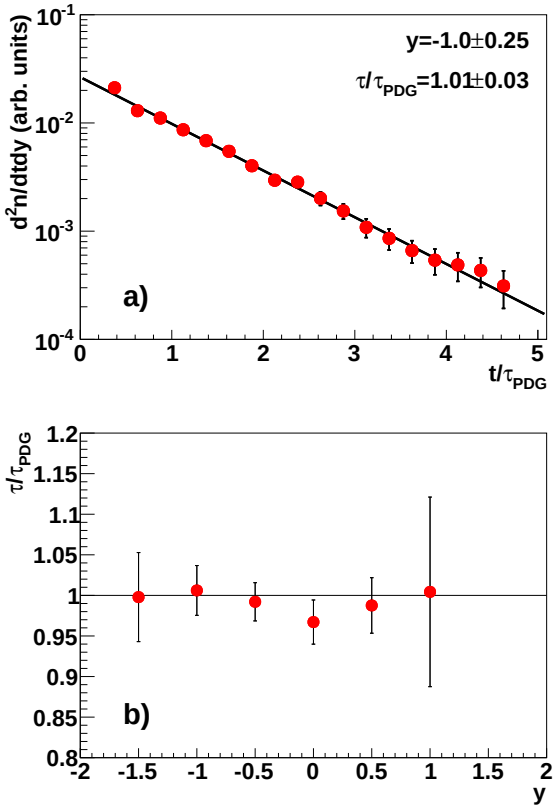

Fig. 10 *Top:* An example of the corrected proper life-time distribution for Λ hyperons produced in inelastic p+p interactions at 158 GeV/c in the rapidity interval y=-1.0±0.25. *Bottom:* The ratio of the fitted mean life-time to its PDG [18] value as a function of rapidity.

These subsets were analysed separately and the results are found to be consistent.

4 Results

4.1 Formalism

The double-differential yields of Λ hyperons in inelastic p+p interactions at 158 GeV/c were calculated in kinematic (k,l) bins (with $k = y$ or x_F, and $l = p_T$ or $m_T - m_\Lambda$) using Eq. (10). The following spectra are presented: $\frac{d^2n}{dydp_T}$, $\frac{d^2n}{dydm_T}$, $\frac{d^2n}{dx_F dp_T}$ and $f_n(x_F, p_T)$, where

$$f_n(x_F, p_T) = \frac{2E^*}{\pi\sqrt{s}} \frac{d^2n}{dx_F dp_T^2} = \frac{1}{\pi\sqrt{s}} \frac{E^*}{p_T} \frac{d^2n}{dx_F dp_T} . \qquad (11)$$

E^* is the energy of the Λ hyperon in the centre of mass system. The weighting factor, E^*/p_T, was calculated at the centre of each (x_F, p_T) bin and is consistent with the average value $\langle E^*/p_T \rangle$ obtained using the EPOS generator.

Single-differential $\frac{dn}{dk}$ distributions are obtained by summing the double-differential yields for a given k over l. In

order to estimate the yield in the unmeasured high p_T range, the function

$$u = \frac{1}{p_T}\frac{d^2n}{dkdp_T} = \frac{1}{m_T}\frac{d^2n}{dkdm_T} = Ae^{-\frac{m_T}{T}} \quad (12)$$

was fitted to the data and integrated beyond the measured p_T, where A denotes the normalisation factor and T the inverse slope parameter. Single-differential invariant yields $F_n(x_F)$ were obtained by performing an integration of Eq. (11) with respect to p_T^2:

$$F_n(x_F) = \int_0^{+\infty} f_n(x_F, p_T)dp_T^2 = \frac{2}{\pi\sqrt{s}}\int_0^{+\infty} E^*\frac{d^2n}{dx_F dp_T}dp_T \ . \quad (13)$$

For the calculation of $F_n(x_F)$, the weighting factor E^* was calculated at the centre of each (x_F, p_T) bin. For the extrapolation into the unmeasured high p_T region Eq. (12) was used.

Invariant cross-section is obtained from $F_n(x_F)$ by multiplying it by the inelastic cross-section σ_{inel}:

$$F(x_F) = \sigma_{inel}F_n(x_F) \ . \quad (14)$$

The mean transverse mass $\langle m_T \rangle$ was calculated from the function Eq. (12) fitted to the m_T distribution as follows:

$$\langle m_T \rangle = \frac{\int_0^{+\infty} m_T u(m_T)dm_T}{\int_0^{+\infty} u(m_T)dm_T}. \quad (15)$$

4.2 Spectra

Double-differential $\frac{d^2n}{dydp_T}$, $\frac{d^2n}{dydm_T}$, $\frac{d^2n}{dx_F dp_T}$ and $f_n(x_F, p_T)$ spectra are shown in Figs. 11 - 14. The numerical values for $\frac{d^2n}{dydp_T}$ and $\frac{d^2n}{dydm_T}$ are presented in Tables 1 and 2, while invariant and non-invariant x_F yields are shown in Table 3 for $x_F < 0$ and Table 4 for $x_F > 0$.

The values of the p_T integrated $\frac{dn}{dy}$ rapidity distribution are presented in Table 5. The table also contains the values of the inverse slope parameter T and the mean transverse mass $\langle m_T \rangle - m_\Lambda$ as function of rapidity. The single-differential x_F distributions are summarised in Table 6. In Sec. 5 below, the obtained single-differential distributions are compared to model predictions and previously published experimental results.

The mean multiplicity of Λ hyperons ($\langle \Lambda \rangle$) was determined from the x_F distribution. As the models applicable in the SPS energies range show large discrepancies in the region not measured by NA61/SHINE (see Fig. 20), the Λ yield in the unmeasured x_F region ($|x_F| > 0.4$) was approximated by the straight line shown in Fig. 20. The line is defined assuming symmetry of the distribution. It crosses the points $A_\pm = \left(\pm 0.35, \frac{1}{2}\left(\frac{dn}{dx_F}(-0.35) + \frac{dn}{dx_F}(0.35)\right)\right)$ and $B_\pm = (\pm 1, 0)$. For the estimation of statistical part of the extrapolation error, the value of the point A was increased/decreased by $\frac{1}{2}\left(\Delta\frac{dn}{dx_F}(-0.35) + \Delta\frac{dn}{dx_F}(0.35)\right)$. The extrapolation amounts to 34.3% of the total Λ yield and results in $\langle \Lambda \rangle = 0.120 \pm 0.006$ $(stat.)$ of the mean Λ multiplicity.

For the EPOS model, not used for this extrapolation, the yield outside of NA61/SHINE acceptance to the total yield amounts to 38.0 %.

The systematic uncertainty of the mean multiplicity was calculated following the procedure described in Sec 3.6. An additional source of systematic uncertainty arises from the extrapolation of the Λ multiplicity to full phase-space. This was estimated by an alternative procedure based on a parametrisation of published rapidity distributions. In an iterative procedure a symmetric polynomial of 4^{th} order [22] was fitted to the $(1/\langle n \rangle)(dn/dz)$ distributions obtained by five bubble-chamber experiments [23–27] and the NA61/SHINE data, where z stands for y/y_{beam}. First, the fit included only the five bubble-chamber datasets. Next, the NA61/SHINE spectrum was normalised to the fit result obtained in the first step and added as the 6^{th} set for the fit. Finally, the procedure was iterated using those six datasets until the normalisation factor converged. The ratio of the integral of the fitted function $\frac{1}{\langle \Lambda \rangle}\frac{dn}{dz}(z) = 0.394 + 1.99z^2 - 2.66z^4$ (see Fig. 15) for the full range of rapidity to the integral in the range outside of the NA61/SHINE acceptance was used as the extrapolation factor for the NA61/SHINE results. This ratio amounted to 1.92 ± 0.12, i.e. 48 % of the total production is outside of the acceptance for this procedure resulting in a mean multiplicity of $\langle \Lambda \rangle = 0.129 \pm 0.008$. The difference between this result and the linear extrapolation of the x_F distribution is added in quadrature to the (positive) systematic error.

The final result for the Λ multiplicity in inelastic p+p interactions at 158 GeV/c then reads as follows:

$$\langle \Lambda \rangle = 0.120 \pm 0.006\ (stat.)\ \pm 0.010\ (sys.)$$

5 Comparison with world data and model predictions

The single-differential spectra from NA61/SHINE are compared in Fig. 15 to results from five bubble-chamber experiments which measured p+p interactions at beam momenta close to 158 GeV/c. The experiments published data for the backward hemisphere, however, with rather small statistics [23–27] and correspondingly large uncertainties. In order to account for the difference in beam momentum the spectra are shown in terms of the scaled rapidity $z = y/y_{beam}$

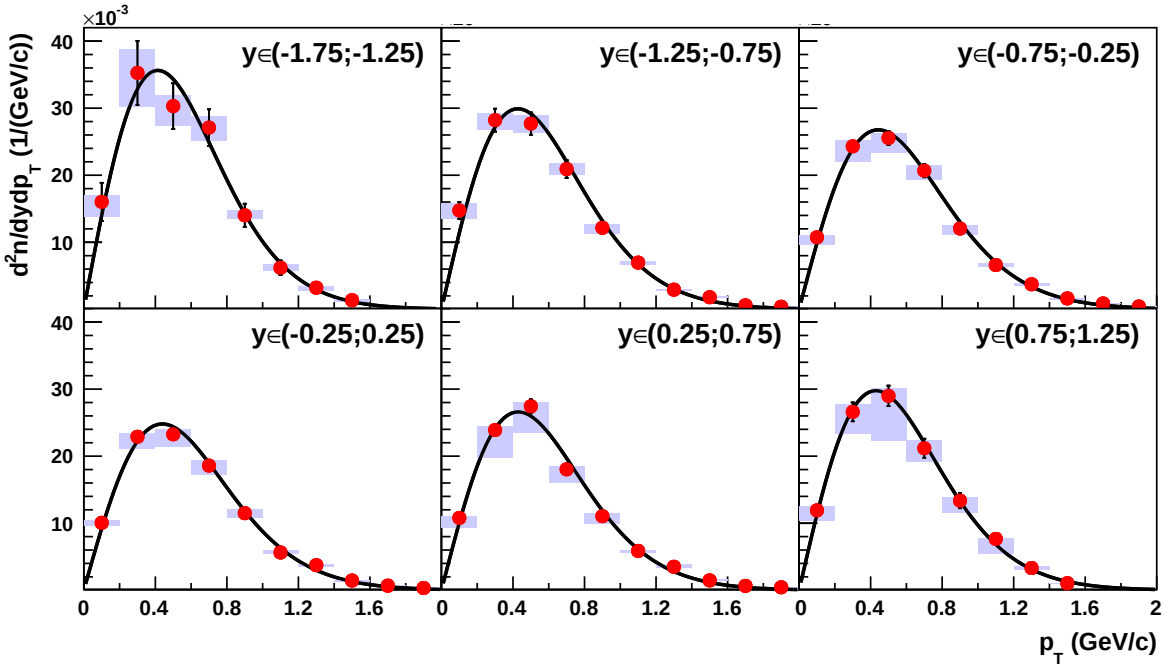

Fig. 11 Spectra $\frac{d^2n}{dydp_T}$ for six bins in rapidity y. The fitted function is given by Eq. (12). The numerical data are listed in the Table 1 and the fitted inverse slope parameter for each of the bins in Table 5.

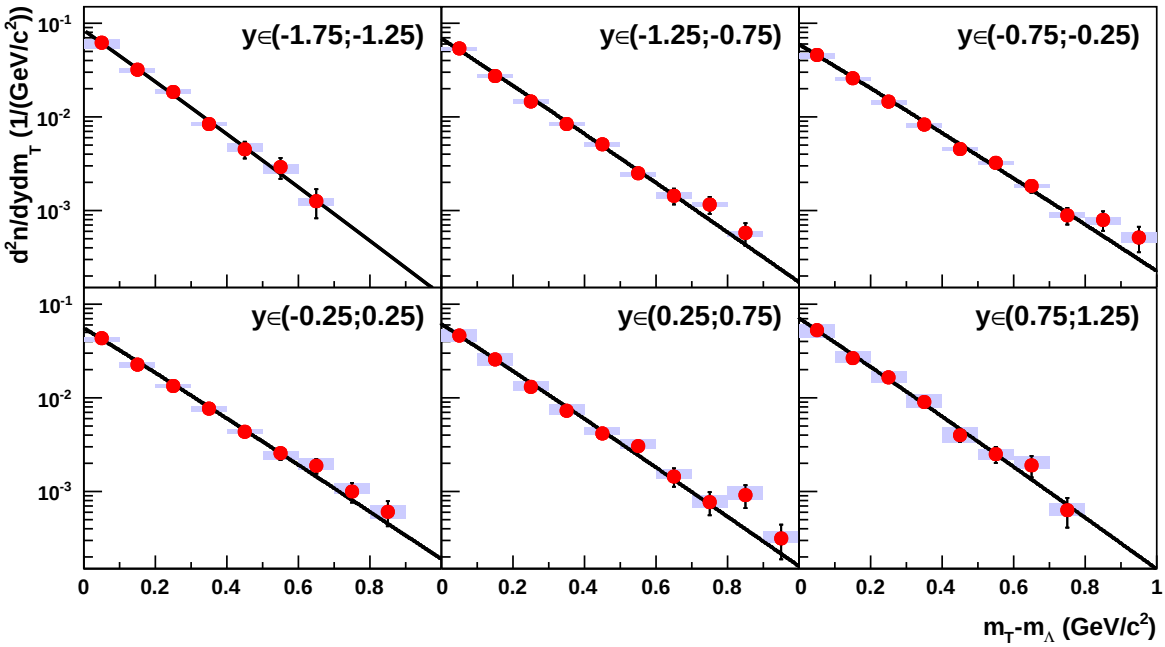

Fig. 12 Spectra $\frac{d^2n}{dydm_T}$ for six bins in rapidity y. The fitted function is given by Eq. (12). The numerical data are listed in Table 2 and the mean transverse mass $\langle m_T \rangle - m_\Lambda$ for each of the bins in Table 5.

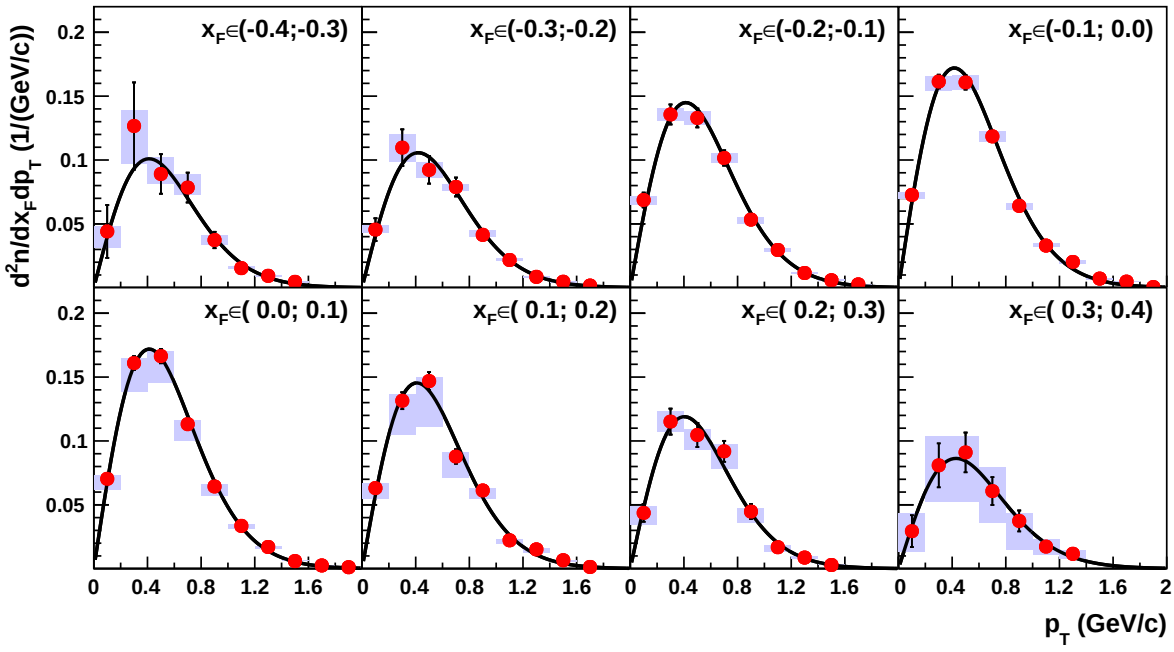

Fig. 13 Spectra $\frac{d^2n}{dx_F dp_T}$ for eight bins in x_F. The fitted function is given by Eq. (12). The numerical data are listed in Table 3 for $x_F > 0$ and in Table 4 for $x_F > 0$.

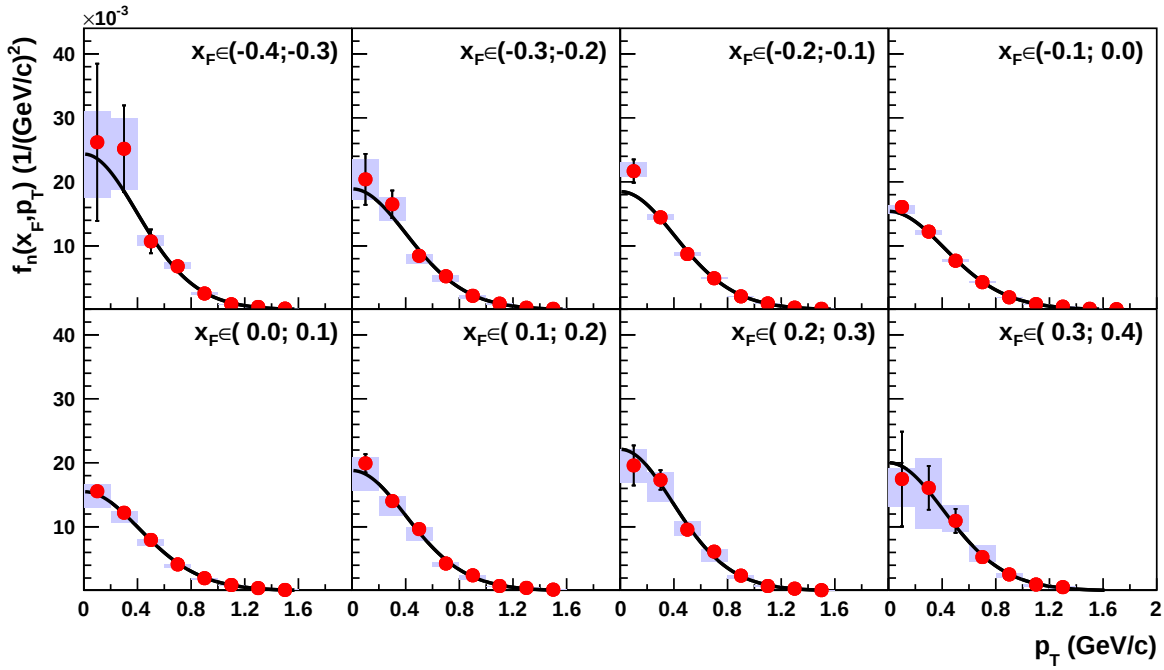

Fig. 14 Spectra f_n for eight bins in x_F. The fitted function was obtained from Eq. (12) by multiplying the right-hand side by p_T. The numerical data are listed in Table 3 for $x_F > 0$ and in Table 4 for $x_F < 0$.

and were normalised to unity in order to compare the shapes. Note, that the same data sets were also used to compute the alternative correction factor used to estimate the systematic uncertainty of $\langle\Lambda\rangle$ (see Sec. 4) obtained by NA61/SHINE.

Though the statistical error and the systematic uncertainty of the NA61/SHINE measurement is much smaller than for the other experiments, and the results are consistent with all the datasets used for the comparison, the general tendency obtained by fitting a symmetric polynomial of 4^{th} order does not describe well the NA61/SHINE data. On the other hand, the result of Brick *et al.* for which the beam momentum (147 GeV/c) differs the least from the NA61/SHINE momentum, shows the best agreement.

The mean multiplicity of Λ for 158 GeV/c inelastic p+p interactions is compared in Fig. 16 with the world data [28] as well as with predictions of the EPOS1.99 model in its validity range. A steep rise in the threshold region is followed by a more gentle increase at higher energies that is well reproduced by the EPOS1.99 model.

The dependence of the invariant spectrum on x_F for NA61/SHINE and published results from bubble chamber experiments [23, 25, 26, 29–31] at nearby beam momenta is shown in Fig. 17. The NA61/SHINE results are consistent with the experiments performed at proton beams of lower energy, although the dip-like structure visible at central x_F in the data from the experiments operating at higher energies is not observed.

Figure 18 shows a comparison of rapidity spectra divided by the mean number of wounded nucleons $1/\langle N_W\rangle$ in inelastic p+p interactions (this paper) and central C+C, Si+Si and Pb+Pb collisions (NA49 [32, 33]) at 158 A GeV/c. The yield of Λ hyperons per wounded nucleon increases with increasing $\langle N_W\rangle$ as a consequence of strangeness enhancement in nucleus-nucleus collisions.

Figure 19 displays m_T spectra at mid-rapidity for inelastic p+p interactions (this paper) and central nucleus-nucleus collisions (NA49 [32, 33]) at 158 A GeV/c. The inverse slope parameter of the spectrum increases with increasing nuclear size due to increasing transverse flow.

A comparison with calculations from the models EPOS1.99 [19], URQMD3.4 [34, 35], and FRITIOF7.02 [36] embedded in HSD2.0 [37] is presented in Fig. 20. The best agreement is found for the EPOS1.99 model.

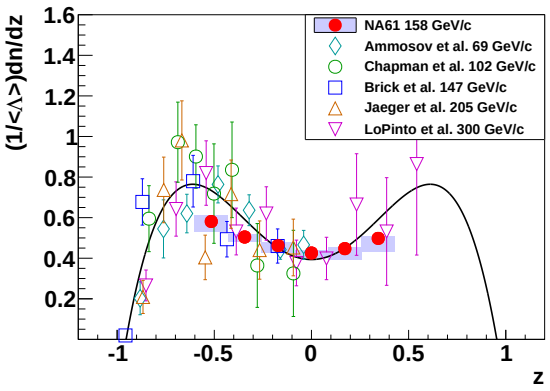

Fig. 15 The scaled Λ yield as function of scaled rapidity $z = y/y_{beam}$ in inelastic p+p interactions measured by NA61/SHINE and selected bubble-chamber experiments [23–27]. The symmetric polynomial of 4^{th} order used for estimation of the systematic uncertainty of Λ mean multiplicity (see Sec. 4.2) is plotted to guide the eye.

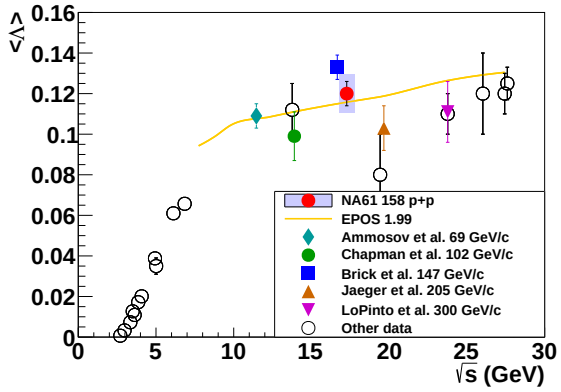

Fig. 16 Collision energy dependence of mean multiplicity of Λ hyperons produced in inelastic p+p interactions. Full symbols indicate bubble chamber results [23–27], the solid red dot shows the NA61/SHINE result. Open symbols depict the remaining world data [28]. The EPOS1.99 [19] prediction is shown by the curve. The systematic uncertainty of the NA61/SHINE result is indicated by the shaded bar.

6 Summary

Inclusive production of Λ-hyperons was measured with the large acceptance NA61/SHINE spectrometer at the CERN SPS in inelastic p+p interactions at beam momentum of 158 GeV/c. Spectra of transverse momentum (up to 2 GeV/c) and transverse mass as well as distributions of rapidity (from -1.75 to 1.25) and x_F (from -0.4 to 0.4) are presented. The mean multiplicity was found to be $0.120 \pm 0.006\,(stat.) \pm 0.010\,(sys.)$. The new results are in reasonable agreement with measurements from bubble-chamber experiments at nearby beam momenta, but have much smaller uncertainties.

Predictions of the EPOS, URQMD and FRITIOF models were compared to the new NA61/SHINE measurements reported in this paper. While EPOS describes the data quite well, significant discrepancies are observed with the latter two models.

The results expand our knowledge of elementary proton-proton interactions, allowing for a more precise description of strangeness production. They are expected to be used not only as an important input in the research of strongly interacting matter, but also as an input for tuning MC-generators,

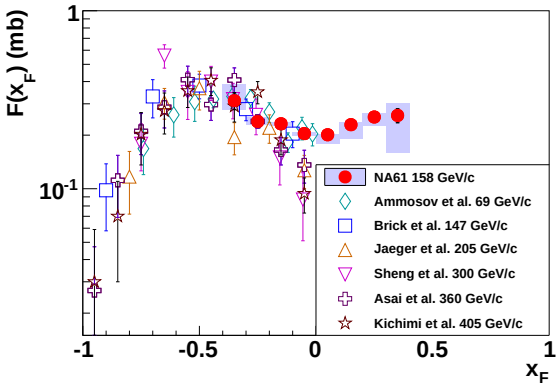
F(x_F) (mb)
x_F
NA61 158 GeV/c
Ammosov et al. 69 GeV/c
Brick et al. 147 GeV/c
Jaeger et al. 205 GeV/c
Sheng et al. 300 GeV/c
Asai et al. 360 GeV/c
Kichimi et al. 405 GeV/c

Fig. 17 Comparison of the invariant x_F spectra (see Eq. (14), $\sigma_{inel.} = 31.8$ mb [18]) from the NA61/SHINE with the data from bubble-chamber experiments at beam momenta close to 158 GeV/c [23, 25, 26, 29–31]. The NA61/SHINE data points are indicated by filled circles. The systematic uncertainty is shown as a band around the points.

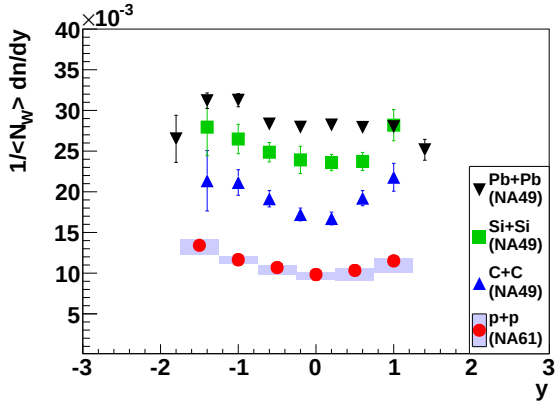

Fig. 18 Rapidity spectra of Λ hyperons divided by the mean number of wounded nucleons in inelastic p+p interactions (NA61/SHINE) and central C+C, Si+Si [32], and Pb+Pb [33] collisions at 158 A GeV/c.

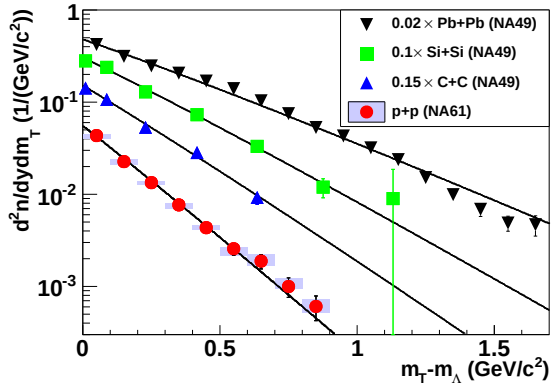

Fig. 19 Spectra of m_T at mid-rapidity ($|y| \leq 0.4$ for A+A, $|y| \leq 0.25$ for p+p) from NA61/SHINE inelastic p+p interactions and central C+C, Si+Si [32], and Pb+Pb [33] collisions for beam momentum of 158 A GeV/c. The lines are fitted using Eq. (12).

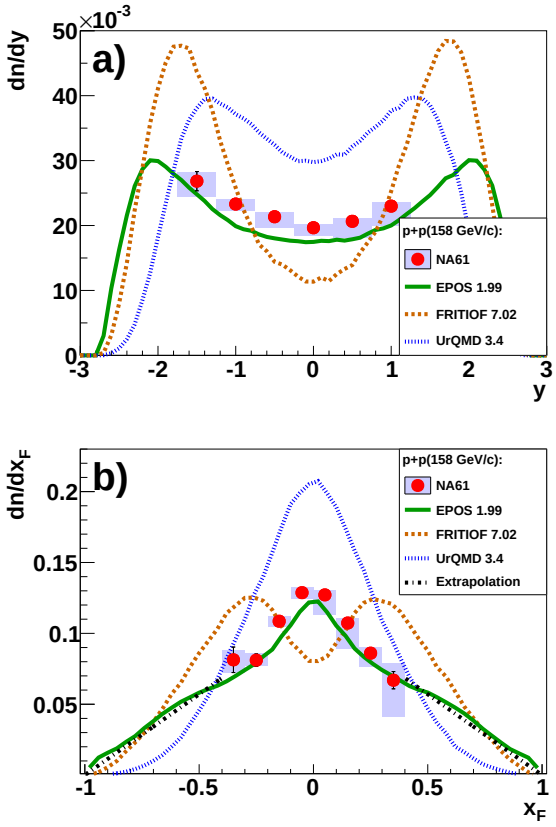

Fig. 20 Comparison of $\frac{dn}{dy}$ (a), and $\frac{dn}{dx_F}$ (b) distributions with calculations of the EPOS [19], URQMD [34, 35] and FRITIOF [36] models. The chain line was used to extrapolate the NA61/SHINE measurements to full phase space. For details see text.

including those used for cosmic-ray shower and neutrino beams simulations.

Acknowledgements

This work was supported by the Hungarian Scientific Research Fund (grants OTKA 68506 and 71989), the János Bolyai Research Scholarship of the Hungarian Academy of Sciences, the Polish Ministry of Science and Higher Education (grants 667/N-CERN/2010/0, NN 202 48 4339 and NN 202 23 1837), the Polish National Science Centre (grants 2011/03/N/ST2/03691, 2012/04/M/ST2/00816 and 2013/11/N/ST2/03879), the Foundation for Polish Science — MPD program, co-financed by the European Union within the European Regional Development Fund, the Federal Agency of Education of the Ministry of Education and Science of the Russian Federation (SPbSU research grant 11.38.193.2014), the Russian Academy of Science and the Russian Foundation for Basic Research (grants 08-02-00018, 09-02-00664 and 12-02-91503-CERN), the Ministry of Education, Culture, Sports, Science and Technology, Japan, Grant-in-Aid for Scientific Research (grants

18071005, 19034011, 19740162, 20740160 and 20039012), the German Research Foundation (grant GA 1480/2-2), the EU-funded Marie Curie Outgoing Fellowship, Grant PIOF-GA-2013-624803, the Bulgarian Nuclear Regulatory Agency and the Joint Institute for Nuclear Research, Dubna (bilateral contract No. 4418-1-15/17), Ministry of Education and Science of the Republic of Serbia (grant OI171002), Swiss Nationalfonds Foundation (grant 200020117913/1) and ETH Research Grant TH-01 07-3. Finally, it is a pleasure to thank the European Organisation for Nuclear Research for strong support and hospitality and, in particular, the operating crews of the CERN SPS accelerator and beam lines who made the measurements possible.

References

1. C. Blume and C. Markert, Prog. Part. Nucl. Phys. **66**, 834 (2011) [arXiv:1105.2798 [nucl-ex]]
2. J. Rafelski and B. Müller, Phys. Rev. Lett. **48**, 1066 (1982)
3. J. Rafelski and B. Müller, Phys. Rev. Lett. **56**, 2334 (1986)
4. M. Gaździcki, M. Gorenstein and P. Seyboth, Acta Phys. Polon. B **42**, 307 (2011) [arXiv:1006.1765 [hep-ph]]
5. M. Gaździcki and P. Seyboth, Acta Phys. Polon. (to appear), [arXiv:1506.08141 [nucl-ex]]
6. N. Abgrall et al. (NA61/SHINE Collaboration), JINST **9**, P06005 (2014)
7. N. Abgrall et al. (NA61/SHINE Collaboration), Phys. Rev. C **84**, 034604 (2011)
8. N. Abgrall et al. (NA61/SHINE Collaboration), Phys. Rev. C **85**, 035210 (2012)
9. N. Abgrall, et al. (NA61/SHINE Collaboration), Phys Rev. C **89**, 025205 (2014)
10. N. Abgrall et al. (NA61/SHINE Collaboration), Eur. Phys. J. C **76**, 84 (2016)
11. N. Abgrall et al. (NA61/SHINE Collaboration), Eur. Phys. J. C **74**, 2794 (2014)
12. C. Boved et al., IEEE Trans. Nucl. Sci. **25**, 572 (1977)
13. A. Wilczek, Ph. D. Thesis, University of Silesia, Katowice, Poland (2015)
14. T Yates et al. (NA49 Collaboration), J. Phys. G **23**, 1889 (1997)
15. K. Levenberg, Q. Appl. Math. **2**, 164 (1944)
16. D. Marquardt, SIAM J. Appl. Math. **11**, 431 (1963)
17. J. Podolanski and R. Armenteros, Philosphical Magazine Series 7, **45:360**, 13 (1953)
18. K.A. Olive et al. (Particle Data Group), Chin. Phys. C **38**, 090001 (2014)
19. K. Werner, F.-M. Liu, and T. Pierog, Phys. Rev. C **74** 044902 (2006)
20. R. Brun, F. Carminati, GEANT Detector Description and Simulation Tool, CERN Program Library Long Writeup W5013 (1993)
21. T. Šuša, Nucl. Phys. A **698**, 491c (2002)
22. M. Gaździcki, and O. Hansen, Nucl. Phys. A **528**, 754 (1991)
23. V.V. Ammosov et al., Nucl. Phys. B **115**, 269 (1976)
24. J.W. Chapman et al., Phys.Lett. **47B**, 465 (1973)
25. D. Brick et al., Nucl. Phys. B **164**, 1 (1980)
26. K. Jaeger et al., Phys. Rev. D **11**, 2405 (1975)
27. F. LoPinto et al., Phys. Rev. D **22**, 573 (1980)
28. M. Gaździcki, and D. Röhrich, Z. Phys. C **71**, 55 (1996)
29. A. Sheng et al., Phys. Rev D **11**, 1733 (1975)
30. M. Asai et al., Z. Phys. C **27**, 11 (1985)
31. H. Kichimi et al., Phys. Rev. D **20**, 37 (1979)
32. C. Alt et al. (NA49 Collaboration), Phys. Rev. Lett. **94**, 052301 (2005)
33. T. Alt et al. (NA49 Collaboration), Phys. Rev. C **78**, 034918 (2008)
34. S. A. Bass et al., Prog. Part. Nucl. Phys. **41**, 225 (1998)
35. M. Bleicher et al., J. Phys. G **25**, 1859 (1999)
36. B. Anderson, G. Gustafson and Hong Pi, Z. Phys. C **57**, 485 (1993)
37. J. Geiss, W. Cassing, and C. Greiner, Nucl.Phys. A **644**, 107 (1998)

Table 1 Double-differential yield $\frac{d^2n}{dydp_T}$.

y	p_T	$\frac{d^2n}{dydp_T}$ $\times 10^3$ $(\frac{1}{GeV/c})$	Δ_{stat}	Δ^-_{sys}	Δ^+_{sys}
-1.5	0.1	16.0	2.8	2.2	1.0
	0.3	35.3	4.8	5.0	3.5
	0.5	30.3	3.4	2.9	1.6
	0.7	27.1	2.7	1.9	1.7
	0.9	14.0	1.7	0.5	0.7
	1.1	6.2	1.1	0.4	0.5
	1.3	3.22	0.71	0.44	0.19
	1.5	1.36	0.45	0.18	0.22
-1.0	0.1	14.7	1.2	1.3	1.1
	0.3	28.2	1.7	1.4	1.1
	0.5	27.7	1.7	1.4	1.2
	0.7	20.9	1.3	0.9	0.8
	0.9	12.16	0.89	0.89	0.46
	1.1	6.96	0.64	0.26	0.22
	1.3	2.93	0.39	0.15	0.12
	1.5	1.80	0.30	0.12	0.13
	1.7	0.59	0.16	0.04	0.04
	1.9	0.38	0.14	0.04	0.02
-0.5	0.1	10.74	0.59	1.11	0.37
	0.3	24.31	0.95	2.34	0.85
	0.5	25.5	1.0	2.2	0.8
	0.7	20.68	1.00	1.41	0.72
	0.9	12.05	0.77	0.96	0.42
	1.1	6.61	0.55	0.28	0.23
	1.3	3.74	0.41	0.18	0.13
	1.5	1.62	0.25	0.12	0.09
	1.7	0.87	0.19	0.07	0.05
	1.9	0.42	0.14	0.06	0.06
0.0	0.1	10.06	0.56	0.47	0.42
	0.3	22.89	0.87	1.75	0.61
	0.5	23.26	0.91	1.83	0.73
	0.7	18.58	0.89	1.44	0.75
	0.9	11.50	0.78	0.66	0.63
	1.1	5.63	0.59	0.20	0.33
	1.3	3.74	0.49	0.22	0.22
	1.5	1.45	0.27	0.09	0.08
	1.7	0.69	0.20	0.05	0.04
	1.9	0.34	0.11	0.06	0.08
0.5	0.1	10.79	0.63	1.55	0.24
	0.3	23.89	0.95	4.07	0.66
	0.5	27.4	1.0	3.9	0.6
	0.7	18.03	0.88	1.94	0.51
	0.9	11.04	0.78	1.13	0.36
	1.1	5.87	0.57	0.27	0.15
	1.3	3.50	0.49	0.14	0.34
	1.5	1.47	0.30	0.14	0.15
	1.7	0.65	0.21	0.09	0.05
	1.9	0.45	0.14	0.46	0.01
1.0	0.1	11.91	0.91	1.55	0.68
	0.3	26.6	1.4	3.2	1.2
	0.5	29.0	1.5	6.6	1.2
	0.7	21.2	1.4	2.1	1.1
	0.9	13.4	1.1	1.7	0.6
	1.1	7.65	0.80	2.26	0.11
	1.3	3.32	0.56	0.20	0.29
	1.5	1.06	0.28	0.00	0.00

Table 2 Double-differential yield $\frac{d^2n}{dydm_T}$.

y	$m_T - m_\Lambda$	$\frac{d^2n}{dydm_T}$ $\times 10^3$ $(\frac{1}{GeV/c^2})$	Δ_{stat}	Δ^-_{sys}	Δ^+_{sys}
-1.5	0.05	62.0	6.2	8.8	4.5
	0.15	31.9	3.2	2.3	1.5
	0.25	18.5	2.1	0.8	1.1
	0.35	8.4	1.3	0.5	0.3
	0.45	4.51	0.92	0.30	0.72
	0.55	2.91	0.73	0.43	0.21
	0.65	1.26	0.43	0.15	0.08
-1.0	0.05	53.8	2.5	2.4	1.7
	0.15	27.3	1.6	1.5	1.1
	0.25	14.6	1.0	0.9	0.7
	0.35	8.40	0.72	0.48	0.31
	0.45	5.10	0.54	0.25	0.34
	0.55	2.50	0.36	0.19	0.08
	0.65	1.44	0.28	0.11	0.14
	0.75	1.16	0.24	0.06	0.08
	0.85	0.58	0.16	0.05	0.03
-0.5	0.05	45.9	1.4	4.3	1.5
	0.15	25.9	1.1	1.7	0.8
	0.25	14.56	0.86	1.04	0.61
	0.35	8.28	0.63	0.63	0.29
	0.45	4.54	0.45	0.21	0.23
	0.55	3.23	0.38	0.19	0.10
	0.65	1.83	0.28	0.07	0.10
	0.75	0.89	0.18	0.05	0.06
	0.85	0.79	0.19	0.09	0.06
	0.95	0.51	0.16	0.06	0.07
0.0	0.05	43.4	1.3	3.0	1.3
	0.15	22.63	0.93	1.82	1.19
	0.25	13.38	0.79	0.66	0.48
	0.35	7.67	0.67	0.68	0.42
	0.45	4.34	0.52	0.20	0.32
	0.55	2.56	0.39	0.39	0.14
	0.65	1.89	0.34	0.19	0.35
	0.75	1.00	0.24	0.06	0.22
	0.85	0.61	0.18	0.09	0.11
0.5	0.05	46.2	1.4	6.9	7.6
	0.15	25.7	1.0	3.5	4.2
	0.25	13.10	0.79	1.12	2.15
	0.35	7.28	0.63	0.76	1.20
	0.45	4.17	0.48	0.13	0.69
	0.55	3.05	0.43	0.17	0.60
	0.65	1.44	0.32	0.09	0.27
	0.75	0.77	0.21	0.10	0.14
	0.85	0.92	0.25	0.11	0.21
	0.95	0.32	0.13	0.03	0.06
1.0	0.05	52.8	2.1	9.4	8.2
	0.15	26.6	1.5	3.0	4.3
	0.25	16.5	1.2	1.9	2.7
	0.35	9.04	0.94	1.19	1.97
	0.45	4.00	0.61	0.67	0.88
	0.55	2.51	0.49	0.31	0.33
	0.65	1.90	0.49	0.16	0.46
	0.75	0.63	0.22	0.08	0.13

Table 3 Double-differential yields, $\frac{d^2n}{x_F p_T}$ and $f_n(x_F, p_T)$, for $x_F < 0$.

x_F	p_T	$\frac{d^2n}{dx_F dp_T}$ $\times 10^3$ $(\frac{1}{GeV/c})$	Δ_{stat}	Δ^-_{sys}	Δ^+_{sys}	$f_n(x_F, p_T)$ $\times 10^3$ $\left(\frac{1}{(GeV/c)^2}\right)$	Δ_{stat}	Δ^-_{sys}	Δ^+_{sys}
-0.35	0.1	44	21	13	4	26	12	9	5
	0.3	127	34	30	12	25.2	6.8	6.4	4.7
	0.5	89	15	8	13	10.7	1.9	0.6	1.0
	0.7	78	12	6	10	6.8	1.0	0.4	0.6
	0.9	37.4	6.4	3.7	4.0	2.56	0.44	0.22	0.19
	1.1	15.4	3.4	0.8	1.0	0.88	0.19	0.06	0.04
	1.3	9.3	2.2	0.8	0.1	0.46	0.11	0.04	0.02
	1.5	4.6	1.5	0.8	0.6	0.201	0.066	0.029	0.042
-0.25	0.1	45.5	8.9	2.0	3.5	20.4	4.0	3.2	3.2
	0.3	110	14	11	10	16.5	2.2	2.6	1.1
	0.5	92	11	6	6	8.44	0.98	1.14	0.32
	0.7	78.9	7.4	2.8	2.3	5.25	0.49	0.94	0.13
	0.9	41.4	4.5	1.4	3.9	2.20	0.24	0.48	0.06
	1.1	21.8	2.8	1.0	1.0	0.97	0.13	0.17	0.04
	1.3	8.5	1.6	0.6	0.6	0.334	0.062	0.077	0.012
	1.5	4.7	1.1	0.3	0.5	0.165	0.038	0.032	0.033
	1.7	1.71	0.58	0.13	0.17	0.055	0.019	0.008	0.005
-0.15	0.1	68.7	5.8	3.7	3.0	21.7	1.8	0.9	1.5
	0.3	135.6	7.8	4.7	5.4	14.46	0.83	0.36	0.46
	0.5	132.9	7.4	5.4	4.9	8.73	0.48	0.30	0.22
	0.7	101.6	6.0	3.4	4.0	4.94	0.29	0.10	0.19
	0.9	53.4	3.9	3.0	1.9	2.11	0.15	0.09	0.05
	1.1	29.6	2.7	1.2	1.3	1.008	0.092	0.033	0.039
	1.3	11.6	1.6	0.6	0.5	0.352	0.049	0.014	0.011
	1.5	5.9	1.1	0.6	0.4	0.165	0.030	0.016	0.015
	1.7	2.64	0.73	0.20	0.11	0.069	0.019	0.005	0.002
-0.05	0.1	72.7	3.4	2.8	2.5	16.08	0.75	1.05	0.26
	0.3	161.4	5.4	6.9	4.5	12.23	0.41	0.43	0.26
	0.5	160.8	5.6	6.3	5.4	7.68	0.27	0.23	0.24
	0.7	118.5	5.2	4.4	3.5	4.33	0.19	0.11	0.07
	0.9	64.1	4.0	2.6	2.2	1.97	0.12	0.06	0.05
	1.1	33.0	2.9	1.2	1.5	0.899	0.078	0.024	0.036
	1.3	20.2	2.3	1.4	1.0	0.506	0.059	0.031	0.036
	1.5	7.2	1.2	0.5	0.4	0.169	0.029	0.016	0.008
	1.7	4.8	1.2	0.3	0.3	0.108	0.027	0.010	0.006
	1.9	0.55	0.32	0.07	0.06	0.0120	0.0070	0.0016	0.0032

Table 4 Double-differential yields, $\frac{d^2n}{x_F p_T}$ and $f_n(x_F, p_T)$, for $x_F > 0$.

x_F	p_T	$\frac{d^2n}{dx_F dp_T}$ $\times 10^3$ $(\frac{1}{GeV/c})$	Δ_{stat}	Δ^-_{sys}	Δ^+_{sys}	$f_n(x_F, p_T)$ $\times 10^3$ $\left(\frac{1}{(GeV/c)^2}\right)$	Δ_{stat}	Δ^-_{sys}	Δ^+_{sys}
0.05	0.1	70.3	3.5	8.9	2.7	15.56	0.77	2.49	1.11
	0.3	160.9	5.4	22.8	3.7	12.20	0.41	1.59	0.15
	0.5	166.4	5.6	20.8	4.0	7.95	0.27	0.97	0.09
	0.7	113.1	4.9	13.3	2.9	4.13	0.18	0.45	0.08
	0.9	64.4	4.2	7.4	1.7	1.97	0.13	0.16	0.04
	1.1	33.5	3.2	2.5	1.0	0.913	0.086	0.065	0.028
	1.3	17.0	2.3	1.1	0.8	0.426	0.058	0.035	0.017
	1.5	6.0	1.3	0.2	0.4	0.141	0.030	0.004	0.009
	1.7	2.56	0.82	0.33	0.14	0.058	0.018	0.007	0.003
	1.9	1.19	0.51	0.21	0.23	0.026	0.011	0.005	0.006
0.15	0.1	63.1	4.5	8.5	3.4	19.9	1.4	4.3	1.0
	0.3	131.5	6.6	26.7	5.1	14.02	0.70	2.28	0.71
	0.5	146.8	7.0	35.4	3.5	9.64	0.46	1.79	0.35
	0.7	87.8	5.7	16.2	3.4	4.27	0.28	0.54	0.19
	0.9	61.2	4.7	6.7	1.8	2.42	0.19	0.62	0.09
	1.1	22.3	2.7	2.4	1.1	0.758	0.091	0.077	0.039
	1.3	15.1	2.5	2.2	1.3	0.460	0.077	0.039	0.043
	1.5	6.6	1.4	1.0	0.4	0.185	0.039	0.032	0.012
	1.7	1.39	0.63	0.14	0.29	0.036	0.017	0.007	0.007
0.25	0.1	43.7	7.0	9.4	5.2	19.6	3.1	2.6	2.6
	0.3	115	10	8	8	17.3	1.5	3.4	1.2
	0.5	104.7	9.4	11.1	4.7	9.57	0.86	1.00	1.20
	0.7	91.9	8.2	13.4	5.4	6.12	0.55	1.58	0.41
	0.9	44.7	5.8	8.9	2.7	2.37	0.31	0.46	0.09
	1.1	16.8	3.3	3.5	1.5	0.75	0.15	0.17	0.05
	1.3	8.7	2.1	0.7	0.8	0.341	0.082	0.039	0.045
	1.5	2.9	1.1	0.4	0.4	0.102	0.037	0.015	0.010
0.35	0.1	29	12	16	14	17.5	7.4	4.3	1.7
	0.3	81	17	28	23	16.1	3.4	6.4	4.6
	0.5	91	16	39	13	10.9	1.9	1.8	2.4
	0.7	61	11	25	19	5.28	0.95	0.81	1.79
	0.9	37.4	8.2	22.3	6.0	2.56	0.56	0.48	0.26
	1.1	17.3	5.1	6.3	6.0	0.99	0.29	0.29	0.13
	1.3	11.7	3.6	4.3	2.6	0.57	0.18	0.18	0.14

Table 5 p_T integrated yield $\frac{dn}{dy}$, the inverse slope parameter T and the mean transverse mass $\langle m_T \rangle - m_\Lambda$.

y	$\frac{dn}{dy}$ $\times 10^3$	Δ_{stat}	Δ^-_{sys}	Δ^+_{sys}	T (MeV)	Δ_{stat}	Δ^-_{sys}	Δ^+_{sys}	$\langle m_T \rangle - m_\Lambda$ $(\frac{GeV}{c^2})$	Δ_{stat}	Δ^-_{sys}	Δ^+_{sys}
-1.5	26.8	1.5	2.4	1.4	143.8	6.3	5.4	3.3	0.156	0.013	0.005	0.006
-1.0	23.30	0.65	1.02	0.73	152.8	3.8	4.2	4.1	0.1687	0.0076	0.0050	0.0046
-0.5	21.35	0.43	1.71	0.64	163.0	3.2	4.5	5.1	0.1813	0.0067	0.0050	0.0056
0.0	19.65	0.40	1.14	0.60	160.7	3.6	4.3	5.2	0.1777	0.0076	0.0051	0.0068
0.5	20.64	0.42	2.53	0.43	154.0	3.6	3.9	8.4	0.1697	0.0070	0.0037	0.0102
1.0	22.98	0.62	2.96	0.65	153.9	4.1	4.0	4.6	0.1640	0.0085	0.0028	0.0084

Table 6 p_T integrated yield $\frac{dn}{x_F}$ and the invariant cross section $F(x_F)$.

x_F	$\frac{dn}{dx_F}$ $\times 10^3$	Δ_{stat}	Δ^-_{sys}	Δ^+_{sys}	$F(x_F)$ $\times 10^3$ (mb)	Δ_{stat}	Δ^-_{sys}	Δ^+_{sys}
-0.35	81.3	9.0	9.3	6.5	313	34	36	70
-0.25	81.1	4.4	3.9	4.7	239	13	10	13
-0.15	108.6	2.9	3.9	3.5	231.6	6.1	5.9	4.9
-0.05	128.7	2.3	4.7	3.7	204.1	3.7	5.2	4.5
0.05	127.2	2.3	14.4	3.0	200.9	3.7	22.3	2.2
0.15	107.3	2.7	18.5	3.0	228.9	5.8	39.2	6.7
0.25	86.0	3.8	9.8	4.0	253	11	29	12
0.35	67.0	6.1	25.8	11.6	258	23	99	45